

Very Strong Superconducting Proximity Effects in PbS Semiconductor Nanowires

Bum-Kyu Kim¹, Hong-Seok Kim¹, Yiming Yang², Xingyue Peng², Dong Yu², Yong-Joo Doh^{1,}*

¹Department of Physics and Photon Science, Gwangju Institute of Science and Technology (GIST), Gwangju, 61005, Korea

²Department of Physics, University of California, Davis, CA 95616, USA

ABSTRACT

We report the fabrication of strongly coupled nanohybrid superconducting junctions using PbS semiconductor nanowires and $\text{Pb}_{0.5}\text{In}_{0.5}$ superconducting electrodes. The maximum supercurrent in the junction reaches up to $\sim 15 \mu\text{A}$ at 0.3 K, which is the highest value ever observed in semiconductor-nanowire-based superconducting junctions. The observation of microwave-induced constant voltage steps confirms the existence of genuine Josephson coupling through the nanowire. Monotonic suppression of the critical current under an external magnetic field is also in good agreement with the narrow junction model. The temperature-dependent stochastic distribution of the switching current exhibits a crossover from phase diffusion to a thermal activation process as the temperature decreases. These strongly coupled nanohybrid superconducting junctions would be advantageous to the development of gate-tunable superconducting quantum information devices.

KEYWORDS: *PbS semiconductor nanowire, superconducting proximity effects, Josephson junction, supercurrent, switching current distribution*

When a semiconductor nanowire (NW) is contacted with two superconducting electrodes, a supercurrent can flow through the nonsuperconducting nanowire because of the superconducting proximity effect.¹ The NW-based superconducting junctions,^{2,3} or nanohybrid Josephson junctions, acquire an advantage of a gate-tunable supercurrent flow by controlling the carrier density in the NW, resulting in a supercurrent-based field-effect transistor.⁴ When the supercurrent is combined with phase-coherent quantum electronic transport in the NW, semiconductor NWs provide a useful platform to develop novel quantum electronic devices, such as gate-tunable superconducting quantum interference devices,^{5,6} Cooper pair splitters,⁷ and quantum electron pumps,⁸ and to explore Majorana fermions,^{9,10} and gate-tunable superconducting qubits.^{11,12}

So far, most of the NW-based superconducting junctions have been made of Al superconducting electrodes with a very low transition temperature at $T_C \sim 1.2$ K. The ultralow transition temperature and very small superconducting gap energy of Al, $\Delta_{Al} \sim 0.15$ meV, result in a relatively small critical current $I_C (\leq 0.1 \mu\text{A})$, which is defined as the maximum supercurrent. Recently, a very short ($L \sim 30$ nm) channel device¹³ of InAs NW contacted with Al electrodes has exhibited a maximum supercurrent up to $I_C \sim 0.8 \mu\text{A}$. Because the Josephson coupling energy $E_J = \hbar I_C / 2e$, where \hbar is Planck constant h divided by 2π and e is the elementary charge, must exceed thermal fluctuations for the observation of nonzero supercurrent, a large critical current would be essential for a wide variety of applications of the NW-based superconducting devices. Although other superconducting electrodes with higher transition temperatures, such as V ($T_C \sim 5.0$ K),¹⁴ Pb ($T_C \sim 7.2$ K),¹⁵ and Nb ($T_C \sim 9.2$ K),¹⁶ have been used to increase the critical current of NW-based superconducting junctions, the improvements ($I_C < 1 \mu\text{A}$) were not significant.

In this work, we demonstrate very strong superconducting proximity effects between a PbS semiconductor NW and PbIn superconducting electrodes. The maximum supercurrent reaches up to $I_C \sim 15 \mu\text{A}$ at $T = 0.3 \text{ K}$, which is, to the best of our knowledge, the highest value for semiconductor-NW-based superconducting junctions. Moreover, the $I_C R_N$ product, which is a figure of merit for a Josephson junction with a normal-state resistance R_N , is larger than the superconducting gap energy of PbIn, resulting in $eI_C R_N / \Delta_{\text{PbIn}} = 1.05$, which is the largest value reported so far for the semiconductor-NW-based superconducting junctions. We also examined the superconducting proximity effects in presence of the microwave and magnetic fields, which are consistent with the theoretical expectations. Furthermore, our measurements of the switching current distribution from the superconducting to resistive branches reveal that the phase diffusion and thermal activation processes are responsible for the stochastic switching behavior, which is dependent on temperature.

RESULTS AND DISCUSSION

The PbS NWs were synthesized using the chemical vapor deposition method in a tube furnace, while the doping of the NWs was modulated by varying the weight ratio of lead chloride and sulfur (see Methods). Figure 1a shows the scanning electron microscopy (SEM) image of the as-grown PbS NWs. The details of NW growth¹⁷ and device fabrication⁶ have been reported elsewhere. A representative SEM image of the PbS NW device is displayed in Fig. 1b, where two neighboring superconducting PbIn electrodes were used to apply the bias current (from I+ to I-) and to measure the voltage difference (between V+ and V-). The diameter w of the PbS NW and the distance L between two superconducting electrodes are found to be 130–200 nm and

180–220 nm, respectively, while the normal-state resistance R_N of the device ranges from 20–130 Ω (see Table S1). The electrical transport properties of the NW devices were measured using a closed-cycle ^3He refrigerator (Cryogenic Ltd.) down to the base temperature of 0.3 K. For the low-noise measurements, two-stage RC filters (cutoff frequency ~ 30 kHz) and π filters were connected in series to the measurement leads.¹⁸

The PbIn superconducting electrode exhibits a superconducting transition below $T_{C,SC} = 7.0$ K upon lowering the temperature, while the supercurrent can flow through the NW junction below $T_{C,JJ} = 3.5$ K for device **D3**, as shown in Fig. 1c. The highest temperature for the observation of the supercurrent was found to be $T = 5.2$ K in PbS NW-based Josephson junctions.⁶ Figure 1d shows the current–voltage (I – V) characteristic curves of devices **D1** and **D2**, displaying hysteresis depending on the sweep direction of the bias current. The switching from the superconductive to dissipative branches occurs at a critical current I_C , while the reversed switching occurs at a return current I_R . The hysteresis can be understood in terms of the presence of an effective capacitance^{19, 20} in the junction or the quasiparticle heating effect.²¹ Here, we note that device **D1** exhibits a maximum switching current $I_C \sim 15$ μA , corresponding to a supercurrent density $J_C \sim 1.1 \times 10^5$ A/cm². To the best of our knowledge, these are the highest I_C and J_C values recorded for the semiconductor-NW-based superconducting junctions,^{13-16, 22} which is rather close to those observed for Au-NW-based junctions.²⁰ For device **D2**, the $eI_C R_N$ product is larger than Δ_{PbIn} , where $\Delta_{\text{PbIn}} = 0.81$ meV is the superconducting gap energy (see discussion below). Table 1 shows a summary of the junction properties for a quantitative comparison.

The differential conductance curve as a function of voltage, $dI/dV(V)$, is shown in Fig. 1e for device **D1** at $T = 0.3$ K. The overshoot of dI/dV near zero voltage is caused by the supercurrent branch, while the dI/dV peaks are attributed to the existence of multiple Andreev reflections²³ (MARs) at the interfaces between the PbIn superconducting electrodes and the PbS semiconductor NW. When an electron coming from the semiconductor is incident upon the highly transparent interface, it can be retro-reflected as a phase-conjugated hole (i.e., the lack of an electron below the Fermi energy) while leaving a Cooper pair in the superconductor, known as the Andreev reflection.¹ When the Andreev reflections occur successively at two superconductor-semiconductor interfaces on the opposite side of the junction, the MARs result in conductance enhancements (or dI/dV peaks) occurring at $V_n^* = 2\Delta/ne$, where n is an integer and Δ is the superconducting gap energy. It is evidently shown that the dI/dV peaks occur at $V_1^* = 1.62$ mV and $V_2^* = 0.81$ mV, indicating $\Delta_{\text{PbIn}} = 0.81$ meV. The temperature dependence of the dI/dV peak positions turns out to be consistent with the Bardeen-Cooper-Schrieffer (BCS) theory of superconductivity¹ (see Fig. S1). Similar features of the subgap structures can be found for different device, implying the transparency at the interface to be $T_{\text{int}} = 0.86$, which is deduced from the excess current (see Fig. S2). We note that this value is higher than those obtained from previous superconducting junctions based on InAs semiconductor NWs.^{2, 13, 16} The large superconducting gap energy of Δ_{PbIn} and formation of highly transparent contacts between the PbIn electrodes and the PbS NW are responsible for the very strong Josephson coupling observed in our experiment. An application of the gate voltage V_G can tune the values of I_C and R_N , as shown in Fig. 1f. Here, the $I_C(V_G)$ and $R_N(V_G)$ data were taken at $T = 2.5$ K and $T = 10.0$ K, respectively. The increase in R_N with decreasing V_G indicates that the PbS NW has a strong n -

type character in the experimental range. Correspondingly, I_C decreases with decreasing V_G , suggesting a nearly constant $I_C R_N$ product over the whole V_G range in this experiment.

The progressive change in the I - V curves with increasing temperature is displayed in Fig. 2a. It is evidently shown that I_C decreases monotonically and the hysteresis becomes reduced at higher temperatures than $T = 1.2$ K. The temperature dependences of I_C and I_R are depicted in Fig. 2b, together with the fitting result for the $I_C(T)$ curve. We fitted $I_C(T)$ to the theoretical expression²⁴ $eI_C R_N = aE_{\text{Th}}[1 - b \exp(-aE_{\text{Th}}/3.2k_B T)]$, where $E_{\text{Th}} = \hbar D/L^2$ is the Thouless energy, and a and b are fitting parameters. The value of E_{Th} is estimated to be 0.19 meV for the channel length $L = 190$ nm and diffusion coefficient⁶ $D = 103$ cm²/s. Thus, the best-fit (the solid-line curve in Fig. 2b) is obtained with $a = 4.6$ and $b = 3$, which are comparable to the parameters in the long and diffusive junction limit²⁴ ($a = 10.8$ and $b = 1.3$). The difference can be explained by that our PbS NW Josephson junction ($E_{\text{Th}}/\Delta_{\text{PbIn}} = 0.23$) is in the intermediate regime between the long- ($E_{\text{Th}}/\Delta_{\text{PbIn}} < 0.01$) and short-junction ($E_{\text{Th}}/\Delta_{\text{PbIn}} > 1$) limits, which is similar to previously studied nanohybrid superconducting junctions.^{18, 20} The superconducting coherence length $\xi = (\hbar D/\Delta_{\text{PbIn}})^{1/2}$ is found to be $\xi = 92$ nm, which is about half of the channel length L .

The existence of genuine Josephson coupling in the PbS NWs can be confirmed by the microwave response of the NW devices. Under microwave irradiation, the I - V curve of the Josephson junction is expected to exhibit quantized voltage plateaus (the so-called Shapiro steps) at $V_n = nhf_{\text{mw}}/2e$, where f_{mw} is the frequency of the external microwave.¹ Figure 3a displays the progressive evolution of the I - V curve for various values of the microwave power P at fixed $f_{\text{mw}} = 10.4$ GHz. The quantized voltage plateaus are clearly observed with the same voltage interval $\Delta V = 21.5$ μV , which is consistent with the theoretical value $hf_{\text{mw}}/2e$. The variation of f_{mw} yields

similar results, as shown in Fig. 3b, where ΔV is linearly proportional to f_{mw} with the slope $h/2e = 2.07 \mu\text{V}/\text{GHz}$ (solid line in the inset). The current width of the n th Shapiro step ΔI_n are depicted in Fig. 3c as a function of $P^{1/2}$, which fit well with the theoretical expression¹ $\Delta I_n = 2I_C |J_n(2eV_{\text{mw}}/hf_{\text{mw}})|$, where J_n is the n th order Bessel function and V_{mw} is the amplitude of the microwave voltage across the junction.

Additional evidence for the Josephson coupling in the PbS NWs can be found in the dependence of I_C on the magnetic field B perpendicular to the substrate. Figure 4a shows the color plot of the differential resistance dV/dI as a function of B and I , where the supercurrent region is denoted by the dark blue color. We note that I_C decreases monotonically with increasing B and vanishes at $B \sim 0.16$ T. The $I_C(B)$ data (symbols) in Fig. 4b is quite different from the conventional expectation of a periodic modulation of I_C with B , i.e., the Fraunhofer diffraction pattern,¹ where the I_C minima occur at the integer magnetic flux quanta in the junction area. Our observations can be explained using the narrow junction model,²⁵ where the applied B field acts as a pair breaker for the Cooper pairs induced in the normal conductor with a junction width w smaller than or comparable to the magnetic length $\zeta_B = (\Phi_0/B_0)^{1/2}$, where $\Phi_0 = h/2e$ is the magnetic-flux quantum and $B_0 = \Phi_0/Lw$ (see Supporting Information). Here, we obtained $\zeta_B = 157$ nm for device **D1** with $w = 130$ nm, satisfying a narrow-junction condition of $w < \zeta_B$. Similar features have also been observed in other narrow superconducting junctions.^{13, 16, 22, 26} Additionally, the I_C hump near zero field is attributed to the magnetic field focusing effect.¹⁵

Another peculiar feature of the $I_C(B)$ data is shown in Fig. 4c for device **D3** with $w = 200$ nm and $\zeta_B = 190$ nm, resulting in $w \gtrsim \zeta_B$. We note that there exist two different types of $I_C(B)$ patterns, both indicated by dV/dI peak structures. The inner structure enclosing the dark blue region resembles a Fraunhofer-type modulation of I_C with B , which is commonly observed in a

wide Josephson junction.¹⁸ It follows the Fraunhofer relation $I_C(B) = I_C(0)|\sin[\pi(\Phi/\Phi_0)]/(\Phi/\Phi_0)|$, where Φ is the magnetic flux through the superconducting junction. Then, the first minimum of I_C is expected to be located at the magnetic field $B_1 = \Phi_0/[(L + 2\lambda)w]$, where λ is the London penetration depth of the superconducting electrodes.¹⁸ Because B_1 is found to be 19 mT, we obtain $\lambda = 180$ nm for the PbIn electrodes, which is comparable to the value obtained in our previous study.⁶ The abrupt switching of $I_C(B)$ above B_1 is attributed to the penetration of magnetic vortices into the PbIn electrodes. The outer dV/dI peak structure, occurring at I_C^* , reveals a monotonic suppression of I_C^* by B , which is consistent with the narrow junction model with $r = 0.53$ (see Supporting Information). Thus, we conclude that the monotonic suppression and periodic modulation of I_C with B can occur simultaneously in intermediate-width ($w \gtrsim \xi_B$) junction.

As displayed in Fig. 5a, the repetition of the current sweep reveals that there exists a stochastic distribution of I_C switching from the superconducting to the resistive branches (see Methods for measurement details). It is well known that the I_C distribution is closely related to the dynamics of the Josephson phase particle in the superconducting junction,¹ where the I_C switching event corresponds to the escape of the phase particle from the local minima of the washboard potential $U(\varphi) = -E_{J0}[\cos(\varphi) + (I/I_{C0})\varphi]$, where φ is the phase difference across the junction, and I_{C0} and E_{J0} ($= \hbar I_{C0}/2e$) are the fluctuation-free I_C and Josephson coupling energy,¹ respectively (see Fig. 5b), with assuming a sinusoidal current-phase relation. Then, the escape is governed by the thermal activation²⁷ (TA), phase diffusion^{28, 29} (PD), and macroscopic quantum tunneling³⁰ (MQT) processes, depending on relative strength of E_{J0} over thermal fluctuations.

Figure 5c shows the I_C distribution data measured at various temperatures, indicating that the sharp I_C distribution obtained at high temperature ($T = 1.2$ K) becomes remarkably broadened at lower temperatures. As a result, the standard deviation of the I_C distribution increases monotonically with decreasing temperature down to $T = 0.46$ K, implying that the PD process is the dominant switching current mechanism in this experiment,³¹ where thermally-activated phase particles are repeatedly retrapped in the neighboring potential minima because of a strong dissipation during the escape. The fitting lines of the switching probability $P(I_C)$ in the PD model are consistent with the observed I_C distribution data, as shown in Fig. 5c. The switching probability is related to the escape rate Γ by $P(I_C) = [\Gamma(I_C)/(dI/dt)] \left\{ 1 - \int_0^{I_C} P(I') dI' \right\}$.²⁷ Here, dI/dt is the sweep rate of the applied current. Figure 5d reveals that the behavior of the current dependence of Γ changes below $T = 0.33$ K, indicating that there occurs a crossover from the PD to the TA regimes as the temperature decreases. The MQT behavior, however, was not observed in our experimental range, in contrast to graphene-based superconducting junctions.^{31, 32} It may be caused by an enhanced electron temperature caused by an incomplete filtering of the high-frequency noise.

CONCLUSIONS

In conclusion, we fabricated and characterized the electronic transport properties of nanohybrid superconducting junctions made of PbS NWs contacted with PbIn superconducting electrodes. We observed the highest values of the critical current and $I_C R_N$ product ever reported in semiconductor-NW-based superconducting junctions. Very strong superconducting proximity effects in PbS NWs are attributed to the formation of highly transparent semiconductor–

superconductor contacts with PbIn electrodes, which yield the relatively large superconducting gap energy. Both the microwave and magnetic field dependences of the I - V characteristics of the PbS-NW superconducting junctions are in good agreement with theoretical expectations. Measurement and analysis of the stochastic distribution of the switching current reveals the underlying mechanism of escape dynamics of the phase particle in the NW-based superconducting junctions.

METHODS

Synthesis. The PbS nanowires (NWs) were synthesized using the chemical vapor deposition method in a horizontal tube furnace (Lindberg Blue M). Lead chloride (PbCl_2 , 99.999%, Alfa Aesar) and Sulfur (S, 99.9999%, Alfa Aesar) powders were placed in the center and outside the heating zone of the furnace, respectively. The growth substrate was prepared using electron-beam evaporation of a 100 nm Ti thin film onto a SiO_2 coated Si wafer. The substrate was placed 5 cm downstream from the center of the heating zone ($T \sim 550^\circ\text{C}$). The synthesis system was first evacuated to a base pressure of 15 mTorr, and then flushed with N_2 (99.999%) three times before filling to atmosphere pressure. The furnace temperature was quickly ramped to 630°C at $60^\circ\text{C}/\text{min}$, while 150 sccm N_2 flow was maintained. At the peak temperature, the quartz boat containing S was transferred to the heating zone to trigger the growth. The growth duration varied from 30 min to 2 h. After the growth, the furnace was naturally cooled down to room temperature over approximately 3 h. The N_2 flow was kept during the entire cooling down process to remove any S residue. The doping of the PbS NWs was modulated by varying the

weight ratio of PbCl_2 and S. The more details of the synthesis, characterization, and doping level control can be found in a previous publication.¹⁷

Device Fabrication and Transport Measurements. For the fabrication of the PbS-NW-based superconducting junctions, the as-grown PbS NWs were transferred onto a highly doped *n*-type silicon substrate covered by a 300-nm-thick oxide layer with a prepatterned bonding pad. The superconducting electrodes were patterned using electron-beam lithography. Prior to the metal evaporation, the NWs were exposed to oxygen plasma to remove any residual resist. To make transparent interfaces, the native oxide layer on the PbS NW surface was etched in 6:1 buffered oxide etchant for 10 s. The superconducting electrodes with $\text{Pb}_{0.5}\text{In}_{0.5}$ (250 nm)/Au (10 nm) were deposited using electron-beam evaporation. A highly doped *n*-type silicon substrate served as the back-gate electrode. Figure 1b shows the scanning electron microscope (SEM) image of a typical PbS-NW-based Josephson junction with a channel length $L = 190$ nm and the four-probe measurement configuration. We also measured the transport properties of 14 devices in three different refrigerator systems: ^3He refrigerator (cryogenic) with a base temperature of $T = 0.3$ K, a 1.5 K cryostat using microwave response, and a 2.5 K cryostat. In particular, the switching current was observed in devices with channel lengths that were less than 250 nm. The detailed parameters of the devices are shown in Table S1. To obtain the switching current distribution, a triangle-wave-shape bias current was applied to the sample with a ramping rate $dI/dt = 240$ $\mu\text{A s}^{-1}$, while 5,000 I_C data were recorded at a threshold voltage $V_{\text{th}} = 30$ μV and a fixed temperature.

ASSOCIATED CONTENT

Supporting Information. The supporting information is available free of charge on the ACS Publications website at <http://pubs.acs.org>.

AUTHOR INFORMATION

Corresponding Author

*E-mail: yjdoh@gist.ac.kr

Notes

The authors declare no competing financial interest.

ACKNOWLEDGMENT

We are grateful to Dr. M.-H. Bae for useful discussions. This work was supported by the U.S. National Science Foundation (Grant No. DMR-1310678) and the National Research Foundation of Korea through the Basic Science Research Program (Grant No. 2015R1A2A2A01006833 and 2015R1A6A3A01020240) and the SRC Center for Quantum Coherence in Condensed Matter (Grant No. 2016R1A5A1008184).

TOC Image:

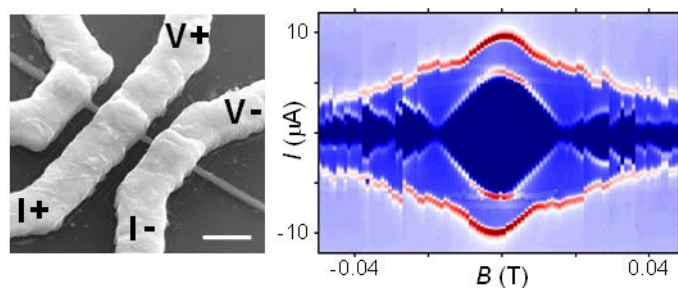


Figure Legends

Table 1. Detailed properties of the PbS NW devices and previously reported nanowire superconducting junctions

Figure 1. SEM images of (a) as-synthesized PbS NWs, and (b) PbS-NW-based junction contacted with PbIn superconducting electrodes. In a four-probe measurement setup, the current bias was driven between I+ and I-. Meanwhile, the voltage drop was measured between V+ and V-. (c) Resistance vs. temperature curve plotted for device **D3**. Superconducting transition temperature of PbIn is $T_{C,SC} = 7.0$ K, while the junction resistance is fully suppressed below $T_{C,JJ} = 3.5$ K. (d) I - V characteristics of devices **D1** and **D2** at $T = 0.3$ K. Here, I_C (I_R) means the switching (retrapping) current. (e) Differential conductance vs. voltage curve for device **D1**. The arrows indicate the subgap conductance peaks (see text). (f) Gate-voltage dependence of I_C and R_N for device **D4**.

Figure 2. (a) Temperature dependence of the I - V characteristic curves for device **D2**. Plots are offset for clarity. (b) Temperature dependences of I_C (circles) and I_R (squares). The solid line is a theoretical calculation of I_C using the long and diffusive junction model (see text).

Figure 3. (a) Microwave-power dependence of the I - V characteristics under the external microwave at the frequency $f_{mw} = 10.4$ GHz. The measurement temperature was $T = 1.5$ K. Voltage plateaus (or Shapiro steps) are clearly observed at $V = V_n$ with $n = 1, 2, 3$. (b) I - V characteristics at $f_{mw} = 4.4, 7.3, 10.4,$ and 15.5 GHz. Here, the voltage axis was normalized by $hf_{mw}/2e$. The inset shows the frequency dependences of the voltage interval, ΔV , data (squares)

and the theoretical prediction (solid line) based on the ac Josephson relation. (c) Current width ΔI_n of the n th Shapiro step ($n = 0, 1$) with respect to the square root of the microwave power ($P^{1/2}$). The solid lines correspond to the theoretical calculations (see text).

Figure 4. (a) Color plot of dynamic resistance dV/dI as a function of I and B at $T = 0.3$ K. The dark blue region corresponds to the supercurrent flow region. (b) Magnetic-field dependence of the I_C data (symbols). The solid line is a fit using the narrow junction model (see text). (c) Color plot of dV/dI for device **D3** at $T = 1.6$ K. (d) The $I_C(B)$ data (red symbols) and I_C^* values corresponding to the first (circles) and secondary (squares) dV/dI peaks, respectively. The red solid line indicates the Fraunhofer pattern in the wide Josephson junction, while the black line represents the fitting result using the narrow junction model.

Figure 5. (a) Repetitive measurement of the stochastic switching current (black lines) and corresponding I_C distribution (red). (b) Schematic diagram of the tilted-washboard potential and the escape processes of a phase particle confined in the potential well. Temperature dependence of the (c) switching current distribution and (d) escaping rate. The solid lines in (c) and (d) are from the theoretical fits to the TA ($T = 0.3$ – 0.33 K) and PD ($T = 0.46$ – 1.2 K) models, respectively.

Table 1.

Sample	I_C (μA)	J_C (kA/cm^2)	$I_C R_N$ (mV)	$eI_C R_N/\Delta$
Pb-based InAs NW¹⁵	0.61	31	0.35	0.26
Al-based InAs NW¹³	0.8	16	0.13	0.98
Nb-based InN NW²²	5.7	50	0.44	0.31
This work (D1)	15	110	0.29	0.36
This work (D2)	7.3	55	0.84	1.05

Figure 1.

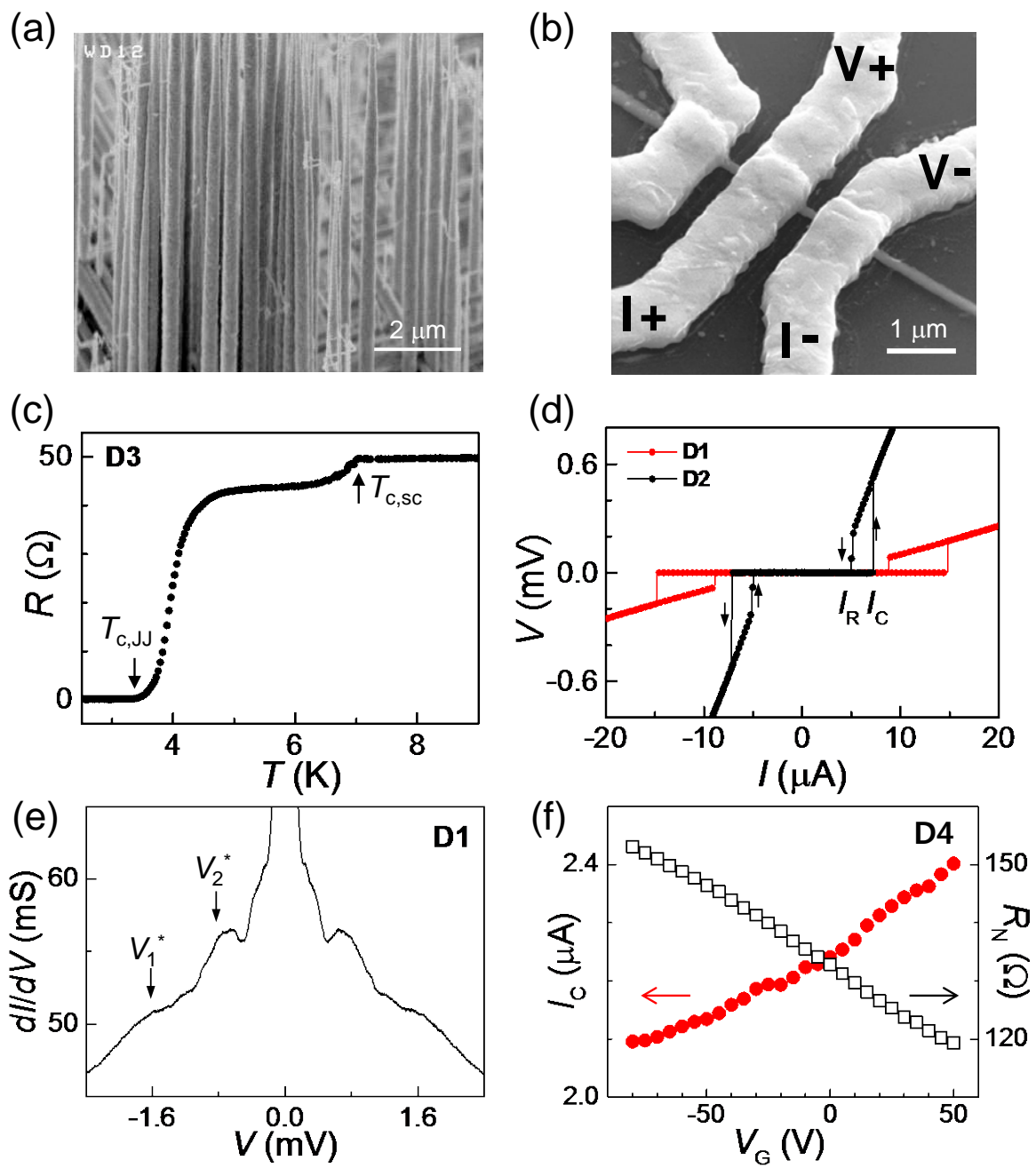


Figure 2.

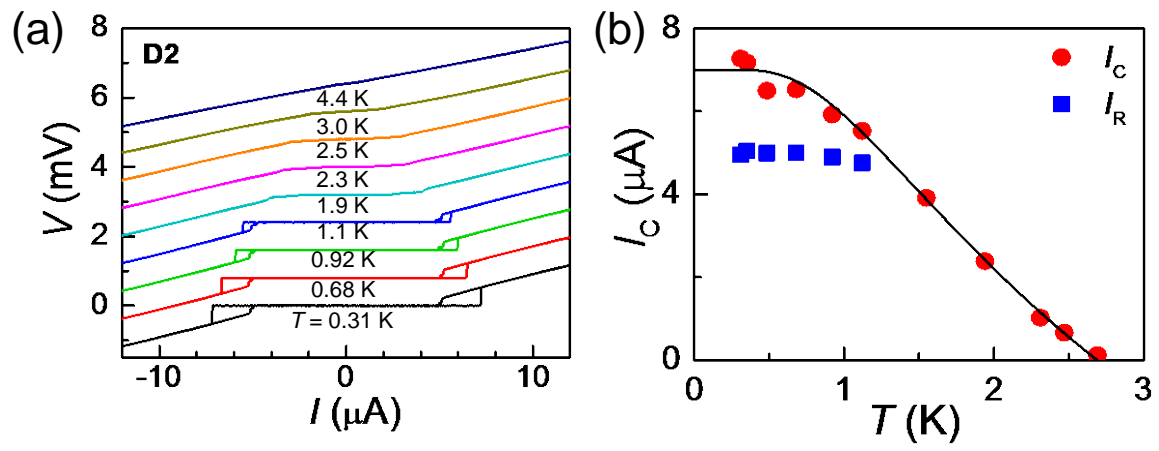


Figure 3.

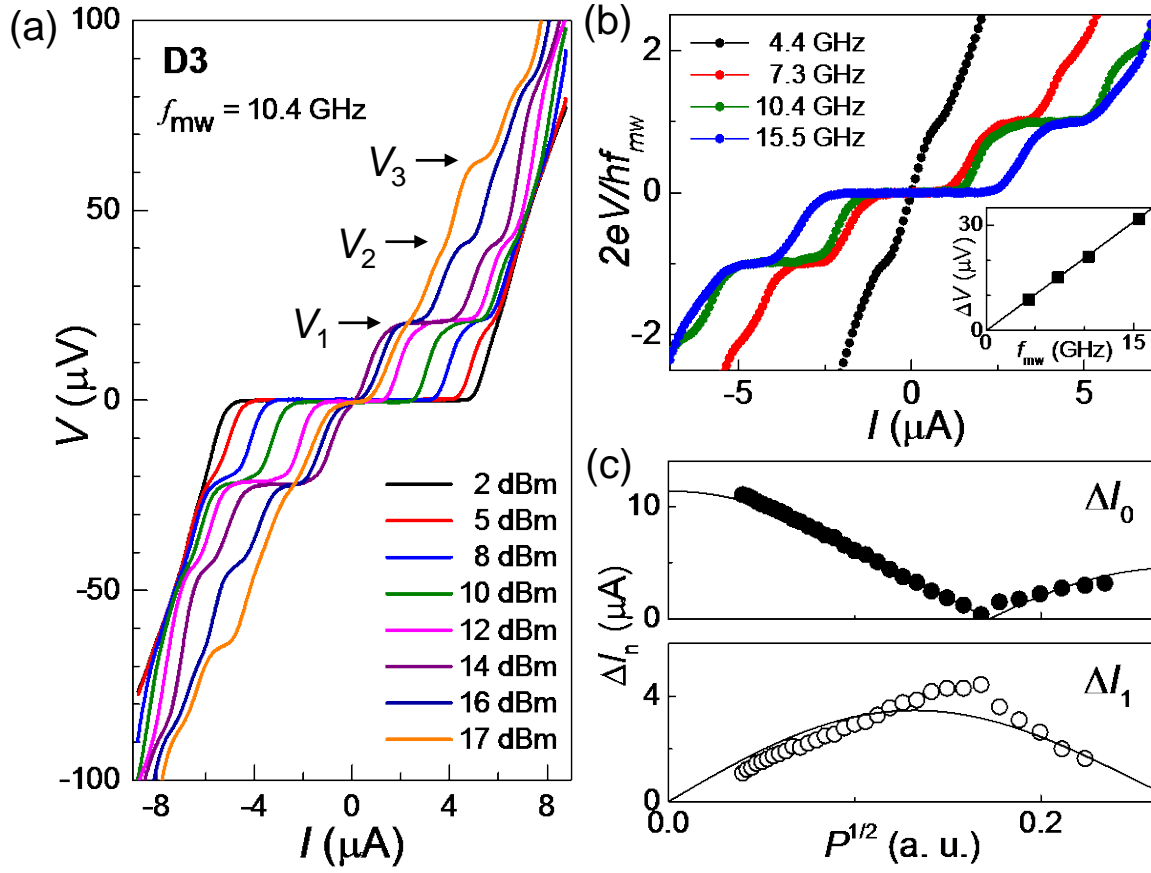


Figure 4.

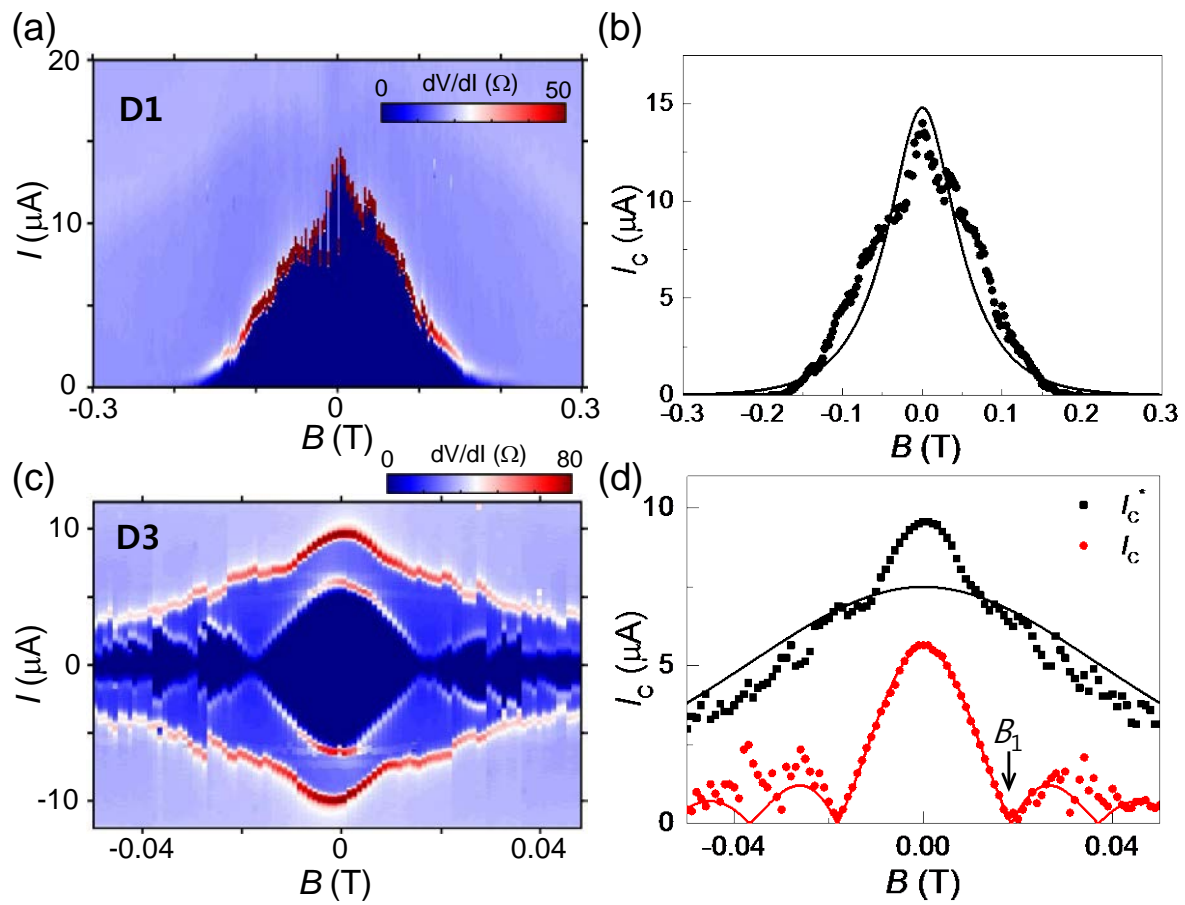
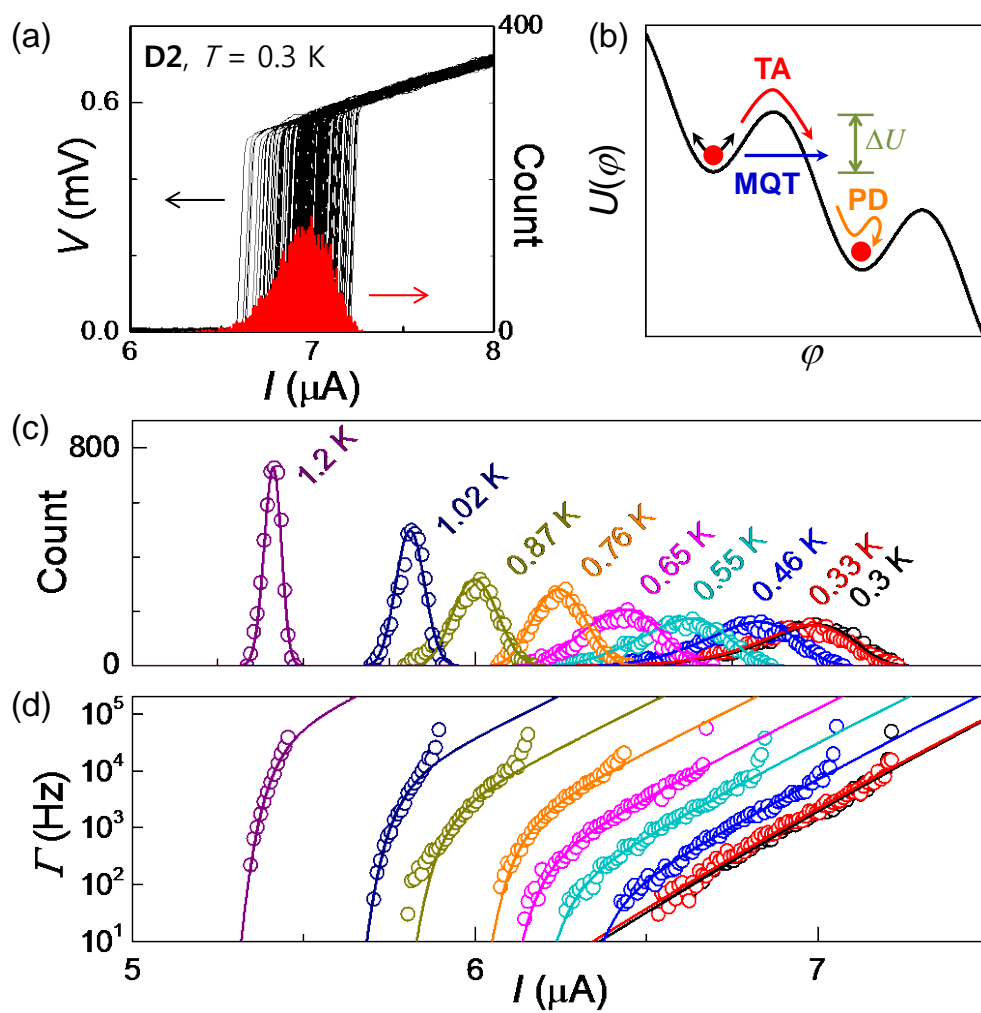


Figure 5.



REFERENCES

1. Tinkham, M. *Introduction to Superconductivity: Second Edition*. Dover Publications: **2004**.
2. Doh, Y.-J.; van Dam, J. A.; Roest, A. L.; Bakkers, E. P. A. M.; Kouwenhoven, L. P.; De Franceschi, S. Tunable supercurrent through semiconductor nanowires. *Science* **2005**, 309, 272-275.
3. Xiang, J.; Vidan, A.; Tinkham, M.; Westervelt, R. M.; Lieber, C. M. Ge/Si nanowire mesoscopic Josephson junctions. *Nat. Nanotechnol.* **2006**, 1, 208-213.
4. Jarillo-Herrero, P.; van Dam, J. A.; Kouwenhoven, L. P. Quantum supercurrent transistors in carbon nanotubes. *Nature* **2006**, 439, 953-956.
5. van Dam, J. A.; Nazarov, Y. V.; Bakkers, E. P. A. M.; De Franceschi, S.; Kouwenhoven, L. P. Supercurrent reversal in quantum dots. *Nature* **2006**, 442, 667-670.
6. Kim, H.-S.; Kim, B.-K.; Yang, Y.; Peng, X.; Lee, S.-G.; Yu, D.; Doh, Y.-J. Gate-tunable superconducting quantum interference devices of PbS nanowires. *Appl. Phys. Express* **2016**, 9, 023102.
7. Hofstetter, L.; Csonka, S.; Nygard, J.; Schonberger, C. Cooper pair splitter realized in a two-quantum-dot Y-junction. *Nature* **2009**, 461, 960-963.
8. Giazotto, F.; Spathis, P.; Roddaro, S.; Biswas, S.; Taddei, F.; Governale, M.; Sorba, L. A Josephson quantum electron pump. *Nat. Phys.* **2011**, 7, 857-861.
9. Mourik, V.; Zuo, K.; Frolov, S. M.; Plissard, S. R.; Bakkers, E. P. A. M.; Kouwenhoven, L. P. Signatures of Majorana fermions in hybrid superconductor-semiconductor nanowire devices. *Science* **2012**, 336, 1003-1007.
10. Das, A.; Ronen, Y.; Most, Y.; Oreg, Y.; Heiblum, M.; Shtrikman, H. Zero-bias peaks and splitting in an Al-InAs nanowire topological superconductor as a signature of Majorana fermions. *Nat. Phys.* **2012**, 8, 887-895.
11. Larsen, T. W.; Petersson, K. D.; Kuemmeth, F.; Jespersen, T. S.; Krogstrup, P.; Nygard, J.; Marcus, C. M. Semiconductor-nanowire-based superconducting qubit. *Phys. Rev. Lett.* **2015**, 115, 127001.
12. de Lange, G.; van Heck, B.; Bruno, A.; van Woerkom, D. J.; Geresdi, A.; Plissard, S. R.; Bakkers, E. P. A. M.; Akhmerov, A. R.; DiCarlo, L. Realization of microwave quantum circuits

using hybrid superconducting-semiconducting nanowire Josephson elements. *Phys. Rev. Lett.* **2015**, 115, 127002.

13. Abay, S.; Nilsson, H.; Wu, F.; Xu, H. Q.; Wilson, C. M.; Delsing, P. High Critical-Current Superconductor-InAs Nanowire-Superconductor Junctions. *Nano Lett.* **2012**, 12, 5622-5625.
14. Spathis, P.; Biswas, S.; Roddaro, S.; Sorba, L.; Giazotto, F.; Beltram, F. Hybrid InAs nanowire-vanadium proximity SQUID. *Nanotechnology* **2011**, 22, 105201.
15. Paajaste, J.; Amado, M.; Roddaro, S.; Bergeret, F. S.; Ercolani, D.; Sorba, L.; Giazotto, F. Pb/InAs Nanowire Josephson Junction with High Critical Current and Magnetic Flux Focusing. *Nano Lett.* **2015**, 15, 1803-1808.
16. Günel, H. Y.; Batov, I. E.; Hardtdegen, H.; Sladek, K.; Winden, A.; Weis, K.; Panaitov, G.; Grützmaker, D.; Schäpers, T. Supercurrent in Nb/InAs-nanowire/Nb Josephson junctions. *J Appl Phys* **2012**, 112, 034316.
17. Yang, Y.; Li, J.; Wu, H.; Oh, E.; Yu, D. Controlled ambipolar doping and gate voltage dependent carrier diffusion length in lead sulfide nanowires. *Nano Lett.* **2012**, 12, 5890-5896.
18. Jeong, D.; Choi, J.-H.; Lee, G.-H.; Jo, S.; Doh, Y.-J.; Lee, H.-J. Observation of supercurrent in PbIn-graphene-PbIn Josephson junction. *Phys. Rev. B* **2011**, 83, 094503.
19. Doh, Y.-J.; De Franceschi, S.; Bakkers, E. P. A. M.; Kouwenhoven, L. P. Andreev Reflection versus Coulomb Blockade in Hybrid Semiconductor Nanowire Devices. *Nano Lett.* **2008**, 8, 4098-4102.
20. Jung, M.; Noh, H.; Doh, Y.-J.; Song, W.; Chong, Y.; Choi, M.-S.; Yoo, Y.; Seo, K.; Kim, N.; Woo, B.-C.; Kim, B.; Kim, J. Superconducting Junction of a Single-Crystalline Au Nanowire for an Ideal Josephson Device. *Acs Nano* **2011**, 5, 2271-2276.
21. Courtois, H.; Meschke, M.; Peltonen, J. T.; Pekola, J. P. Origin of hysteresis in a proximity Josephson junction. *Phys. Rev. Lett.* **2008**, 101, 067002.
22. Frielinghaus, R.; Batov, I. E.; Weides, M.; Kohlstedt, H.; Calarco, R.; Schäpers, T. Josephson supercurrent in Nb/InN-nanowire/Nb junctions. *Appl. Phys. Lett.* **2010**, 96, 132504.
23. Klapwijk, T. M.; Blonder, G. E.; Tinkham, M. Explanation of subharmonic energy gap structure in superconducting contacts. *Physica B+C* **1983**, 109 & 110B, 1657-1664.
24. Dubos, P.; Courtois, H.; Pannetier, B.; Wilhelm, F. K.; Zaikin, A. D.; Schon, G. Josephson critical current in a long mesoscopic S-N-S junction. *Phys. Rev. B* **2001**, 63, 064502.

25. Cuevas, J. C.; Bergeret, F. S. Magnetic interference patterns and vortices in diffusive SNS junctions. *Phys. Rev. Lett.* **2007**, *99*, 217002.
26. Angers, L.; Chiodi, F.; Montambaux, G.; Ferrier, M.; Gueron, S.; Bouchiat, H.; Cuevas, J. C. Proximity dc squids in the long-junction limit. *Phys. Rev. B* **2008**, *77*, 165408.
27. Fulton, T. A.; Dunkleberger, L. N. Lifetime of Zero-Voltage State in Josephson Tunnel-Junctions. *Phys. Rev. B* **1974**, *9*, 4760.
28. Männik, J.; Li, S.; Qiu, W.; Chen, W.; Patel, V.; Han, S.; Lukens, J. E. Crossover from Kramers to phase-diffusion switching in moderately damped Josephson junctions. *Phys. Rev. B* **2005**, *71*, 220509.
29. Krasnov, V. M.; Bauch, T.; Intiso, S.; Hürfeld, E.; Akazaki, T.; Takayanagi, H.; Delsing, P. Collapse of thermal activation in moderately damped Josephson junctions. *Phys. Rev. Lett.* **2005**, *95*, 157002.
30. Clarke, J.; Cleland, A. N.; Devoret, M. H.; Esteve, D.; Martinis, J. M. Quantum-Mechanics of a Macroscopic Variable - the Phase Difference of a Josephson Junction. *Science* **1988**, *239*, 992-997.
31. Lee, G.-H.; Jeong, D.; Choi, J.-H.; Doh, Y.-J.; Lee, H.-J. Electrically Tunable Macroscopic Quantum Tunneling in a Graphene-Based Josephson Junction. *Phys. Rev. Lett.* **2011**, *107*, 146605.
32. Choi, J.-H.; Lee, G.-H.; Park, S.; Jeong, D.; Lee, J.-O.; Sim, H.-S.; Doh, Y.-J.; Lee, H.-J. Complete gate control of supercurrent in graphene p-n junctions. *Nat. Commun.* **2013**, *4*, 2525.

Very Strong Superconducting Proximity Effects in PbS Semiconductor Nanowires

Bum-Kyu Kim¹, Hong-Seok Kim¹, Yiming Yang², Xingyue Peng², Dong Yu², Yong-Joo Doh^{1,}*

¹Department of Physics and Photon Science, Gwangju Institute of Science and Technology (GIST), Gwangju, 61005, Korea

²Department of Physics, University of California, Davis, CA 95616, USA

Supporting Information

1. Table S1. Parameters of nanowires
2. Figure S1. Temperature dependence of Δ_{PbIn}
3. Figure S2. Excess current and multiple Andreev reflections
4. Figure S3. Fitting to TA and PD models
5. Fitting to the narrow junction model
6. Fitting to switching current models

*Address correspondence to yjdoh@gist.ac.kr

Table S1. Physical parameters of PbS nanowire samples.

No.	Channel length (nm)	Width (nm)	I_C (μA)	Base temperature (K)	R_N (Ω)
D1	190	130	15	0.3	21
D2	190	130	7.3	0.3	120
D3	180	200	5.9	1.5	49
D4	185	125	3.2	2.6	130
D5	3000	140	0	0.3	133

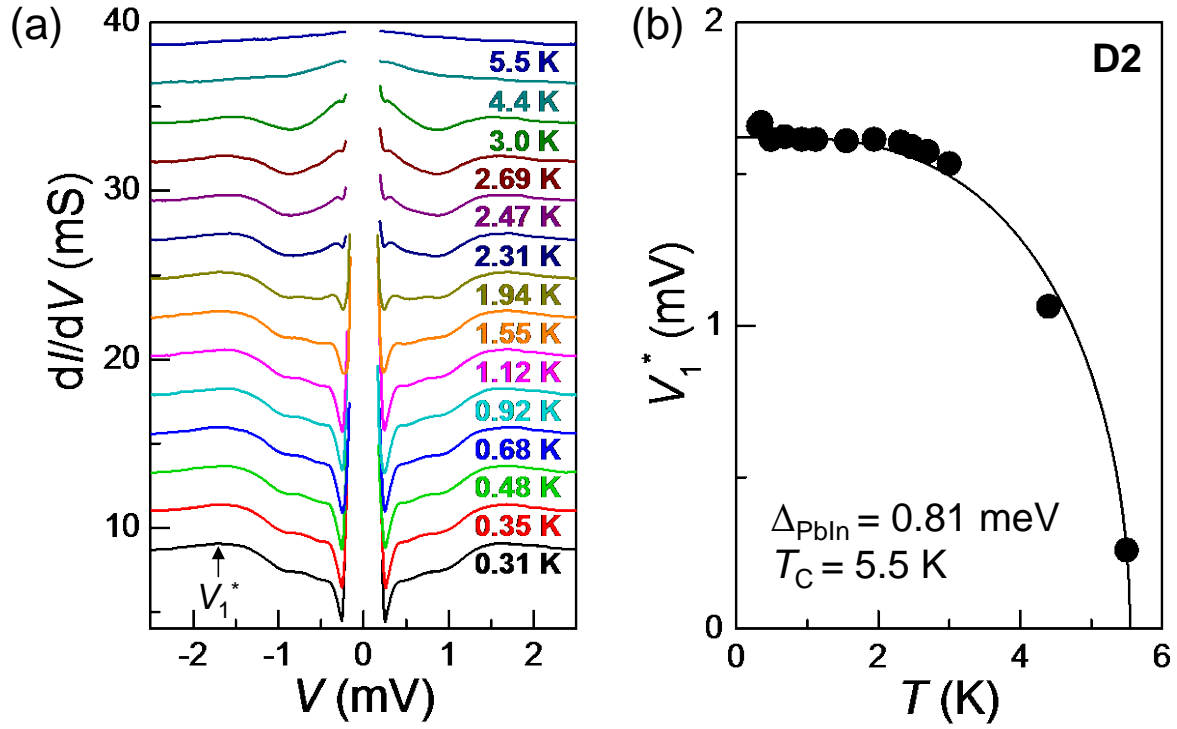


Figure S1. (a) Temperature dependence of dI/dV vs. V curve. Overshoot behavior near zero bias voltage is not shown here for clarity. (b) Temperature dependence of V_1^* (symbols), corresponding to Δ_{pbln}/e . The solid line is a fit to the BCS theory.

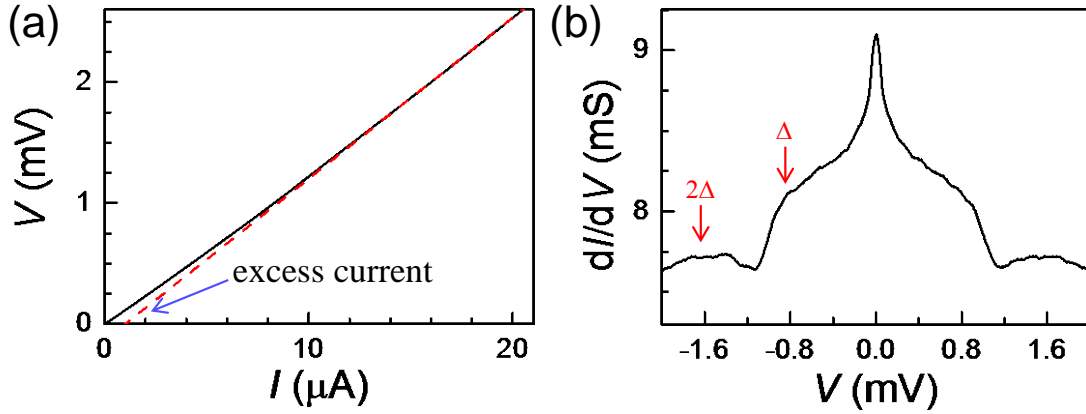


Figure S2. (a) I - V characteristic of PbS NW-based superconducting junction (**D5**) at $T = 300$ mK. The excess current, which is the zero-voltage crossing point of the extrapolated line of the I - V curve at the high bias ($eV > 2\Delta_{\text{PbIn}}$) region, is obtained to be $I_{\text{exc}} = 1 \mu\text{A}$. The transparency at the interface is estimated to be $T_{\text{int}} = 0.86$.¹ (b) Corresponding differential conductance dI/dV vs. V plot. Multiple Andreev reflections result in the dI/dV peaks occurring at $V^* = \Delta_{\text{PbIn}}/e$ and $2\Delta_{\text{PbIn}}/e$. Note that the conductance enhancement was observed from a very long channel ($L = 3 \mu\text{m}$) device, although no supercurrent was observed in **D5**.

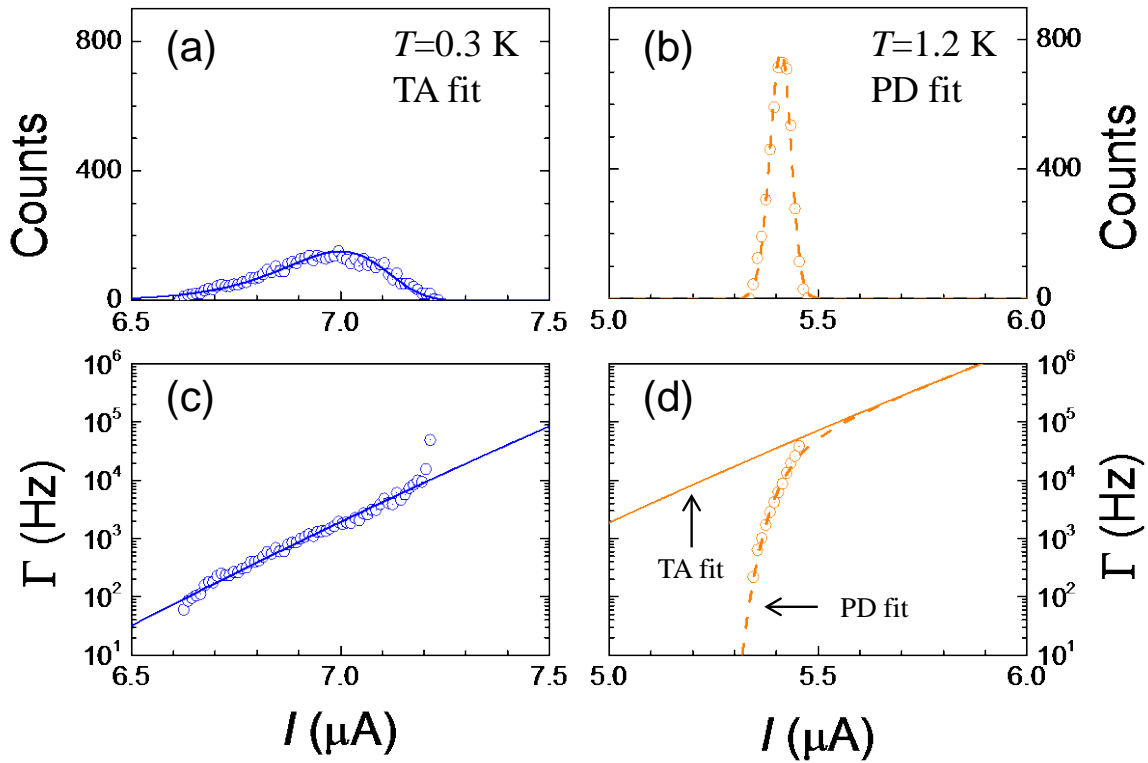


Figure S3. Fitting to the TA and PD models. Experimental data (symbols) of the switching current distribution and best-fit results (lines) at (a) $T = 0.3$ K and (b) 1.2 K, respectively. In the TA regime at $T = 0.3$ K, $P(I_C)$ shows a characteristic tail feature at the left side, while $P(I_C)$ in the PD regime exhibits a relatively symmetric and sharper distribution. (c-d) Corresponding escape rate $\Gamma(I_C)$ data (symbols) and best-fit results (solid lines for TA and dashed for PD model) at $T = 0.3$ K and 1.2 K, respectively.

Fitting to the narrow junction model

Using this model,² the monotonically decreasing I_C can be expressed as

$$eRI_C = \frac{4\pi k_B T}{r} \sum_{n=0}^{\infty} \frac{\Delta^2 / (\Delta^2 + \omega_n^2)}{\sqrt{2 \left(\frac{\omega_n + \Gamma_B}{E_{Th}} \right)} \sinh \sqrt{2 \left(\frac{\omega_n + \Gamma_B}{E_{Th}} \right)}}$$

where $\Gamma_B = De^2 B^2 w^2 / 6\hbar$ is the magnetic depairing energy, $\omega_n = \pi k_B T (2n + 1)$ is the n th Matsubara energy, $r = R_B / R_N$, and R_B is the barrier resistance. The black solid line in Fig. 4b (Fig. 4d) is the fitting result with $r = 1.43$ (0.53), while $\Delta_{PbIn} = 0.81$ meV and $D = 103$ cm²/s are fixed.

Fitting to switching current models

In TA regime,³ switching event from superconducting to resistive branch occur thermally activated escape of phase particle in a tilted-washboard potential. The escape rate Γ_{TA} is expressed by $\Gamma_{TA} = a_t(\omega_p/2\pi)\exp[-\Delta U/k_B T]$, where damping-dependent factor $a_t = (1+1/4Q^2)^{1/2} - 1/2Q$, tilted washboard potential barrier $\Delta U = 2E_{J0}[(1-\gamma^2)^{1/2} - \gamma \cos^{-1} \gamma]$, normalized current $\gamma = I/I_{C0}$, Josephson plasma frequency $\omega_p = \omega_{p0}(1-\gamma^2)^{1/4}$, the plasma frequency in zero bias current $\omega_{p0} = (2eI_{C0}/\hbar C)^{1/2}$, and quality factor $Q = 4I_C/\pi I_R$. In this work, the geometrical junction capacitance C was replaced by the effective capacitance $C_{eff} = \tau/R_N$, where electron diffusion time $\tau = \hbar/E_{Th}$, Thouless energy $E_{Th} = \hbar D/L^2$, diffusion constant $D = v_F l/3$, the Fermi velocity v_F , and the mean free path l .

In the PD regime,^{4,5} a thermally activated phase particle to escape at low bias current regime is repeatedly retrapped in the neighboring potential well due to a strong dissipation. Thus the escape rate Γ_{PD} is given⁴ by $\Gamma_{PD} = \Gamma_{TA}(1-P_{RT})\ln(1-P_{RT})^{-1}/P_{RT}$. The retrapping probability P_{RT} is obtained by integrating the retrapping rate $\Gamma_{RT} = \omega_{p0}[(I_{R0})/I_{C0}](E_{J0}/2\pi k_B T)^{1/2} \exp(-\Delta U_{RT}/k_B T)$, where $\Delta U_{RT} = (E_{J0}Q_0^2/2)[(I-I_{R0})/I_{C0}]^2$ is the retrapping barrier with $Q_0 = 4I_{C0}/\pi I_{R0}$ and I_{R0} is the fluctuation-free retrapping current.^{6,7}

Supplementary Reference

1. Flensberg, K.; Hansen, J. B.; Octavio, M. Subharmonic energy-gap structure in superconducting weak links. *Phys. Rev. B* **1988**, 38, 8707.
2. Cuevas, J. C.; Bergeret, F. S. Magnetic interference patterns and vortices in diffusive SNS junctions. *Phys. Rev. Lett.* **2007**, 99, 217002.
3. Fulton, T. A.; Dunkleberger, L. N. Lifetime of Zero-Voltage State in Josephson Tunnel-Junctions. *Phys. Rev. B* **1974**, 9, 4760.
4. Männik, J.; Li, S.; Qiu, W.; Chen, W.; Patel, V.; Han, S.; Lukens, J. E. Crossover from Kramers to phase-diffusion switching in moderately damped Josephson junctions. *Phys. Rev. B* **2005**, 71, 220509.
5. Krasnov, V. M.; Bauch, T.; Intiso, S.; Hürfeld, E.; Akazaki, T.; Takayanagi, H.; Delsing, P. Collapse of thermal activation in moderately damped Josephson junctions. *Phys. Rev. Lett.* **2005**, 95, 157002.
6. Krasnov, V. M.; Golod, T.; Bauch, T.; Delsing, P. Anticorrelation between temperature and fluctuations of the switching current in moderately damped Josephson junctions. *Phys. Rev. B* **2007**, 76, 224517.
7. Bae, M.-H.; Sahu, M.; Lee, H.-J.; Bezryadin, A. Multiple-retrapping processes in the phase-diffusion regime of high-T_c intrinsic Josephson junctions. *Phys. Rev. B* **2009**, 79, 104509.